Doping-induced singlet-to-triplet superconducting transition in $Ba_2CuO_{3+\delta}$

Priyo Adhikary,[1,2] Mayank Gupta,[1,3] B. R. K. Nanda,[1,3,*] and Shantanu Mukherjee[1,2,†]

[1]*Center for Atomistic Modelling and Materials Design, Indian Institute of Technology Madras, Chennai 600036, India*

[2]*Department of Physics, Indian Institute Of Technology Madras, Chennai 600036, India*

[3]*Condensed Matter Theory and Computational Lab, Department of Physics, Indian Institute Of Technology Madras, Chennai 600036, India*

(Received 20 February 2024; revised 24 May 2024; accepted 24 May 2024; published 5 June 2024)

In this paper, we perform a numerical simulation on the recently discovered high-temperature superconductor ($T_c = 73$ K) $Ba_2CuO_{3.2}$ while focusing on doping dependence of alternating CuO_6 octahedra and CuO chainlike states. Employing the multiband random phase approximation, we compute the spin-fluctuation mediated pairing interaction, subsequently determining its pairing eigenvalues and eigenfunctions relative to oxygen-doping levels. We find that, for the certain range of hole doping in $Ba_2CuO_{3+\delta}$, a singlet $d_{x^2\text{-}y^2}$-wave pairing symmetry emerges if we keep the doping below the critical value x_c. Interestingly, upon hole doping, the dominant pairing symmetry undergoes a transition to a triplet (odd paring) type from the singlet state. This change in pairing is driven by the competition between the nesting vectors coming from the Fermi surface of d_{z^2} and $d_{x^2\text{-}y^2}$ orbitals within the CuO_6 octahedra. This triplet state is attainable through hole doping, while suppressing interlayer self-doping effects. Furthermore, we present the density of states within the superconducting phase, offering a potential comparison with tunneling spectra in $Ba_2CuO_{3+\delta}$. Our research provides insights into the intricate pairing symmetries in $Ba_2CuO_{3+\delta}$ and their underlying pairing mechanisms.

DOI: 10.1103/PhysRevB.109.224503

I. INTRODUCTION

One of the intriguing features of cuprate superconductors is the possibility of d-wave pairing symmetry, that leads to a superconducting (SC) gap with nodes on the Fermi surface (FS) [1–3]. However, recent experiments have pointed toward the possibility of a nodeless pairing state in certain electron- and hole-doped regions of the cuprate high-T_c superconductors [4–14]. This deviation from a d-wave nature of the SC gap suggests a more complex phase diagram of cuprates than previously considered [15]. Theoretical studies have also shown that a triplet state can emerge in cuprates within both one- and three-band models [16,17], depending on the doping level and the interaction parameters. However, there is no direct experimental evidence for a triplet state in cuprates so far. It is within this context that the recent discovery of SC in $Ba_2CuO_{3+\delta}$ (BCO) [18] becomes particularly significant, as it may provide a platform to explore the nature of the pairing symmetry in cuprates.

The unit cell of $Ba_2CuO_{3.25}$ has two primary layers: I and II. Layer I exhibits octahedral and square planar Cu-O complexes alternately stacked along the b direction, and layer II has only square planar complexes along the b axis, see Fig. 1(a). This two-layer feature originates from the missing oxygen atoms in the Ba_2CuO_4 lattice. The oxygen k-edge x-ray absorption spectra [18,19] have provided evidence that points toward such a layered arrangement. In a recent study, we have examined the electronic structure of $Ba_2CuO_{3.25}$ [20] and have shown with electronic structure calculations that the interlayer hybridization has a pronounced effect on the effective band structure, leading to a shift in the Van Hove singularity (VHS), and the $d_{x^2\text{-}y^2}$ orbital moves below the Fermi level [21]. However, as we increase the hole doping, the $d_{x^2\text{-}y^2}$ orbital crosses the Fermi level and contributes significantly to the VHS. This is crucial for determining the pairing symmetry in BCO.

In this paper, we investigate the variations in SC pairing symmetry and strength as a function of hole doping. We consider a 14-orbital basis, which is subsequently downfolded to a five-orbital basis [20]. This includes the d_{z^2} and $d_{x^2\text{-}y^2}$ orbitals from the CuO_6 octahedra of the Cu(1) atom in layer I and the $d_{b^2\text{-}c^2}$ orbital from the chain state of the Cu(2) atom in layer I and the Cu(3)/Cu(4) atoms in layer II. This Hamiltonian accurately replicates the low-energy bands observed in density functional theory (DFT) calculations. Notably, due to octahedral compression, the Cu-$d_{x^2\text{-}y^2}$ orbital is positioned below the Fermi level, see Fig. 1(b). As we increase hole doping, this orbital becomes crucial in determining the SC pairing symmetry. Our model assumes that SC pairing interactions arise from spin-fluctuation mechanisms, incorporating multiband Hubbard interactions within the framework of the weak coupling random phase approximation (RPA). The most robust solution of this pairing interaction indicates a dominant SC gap. The dominant pairing strength in the singlet channel originates from a nesting vector of $\pm(\pi\text{-}\delta, \pi\text{-}\delta)$. Consequently, the SC gap function changes sign between momentum vectors connected by this nesting vector, leading to a $d_{x^2\text{-}y^2}$ pairing symmetry.

Prompted by the recent discovery of SC in BCO at high doping level (40%), we aim to elucidate the SC pairing

*Contact author: nandab@iitm.ac.in

†Contact author: shantanu@iitm.ac.in

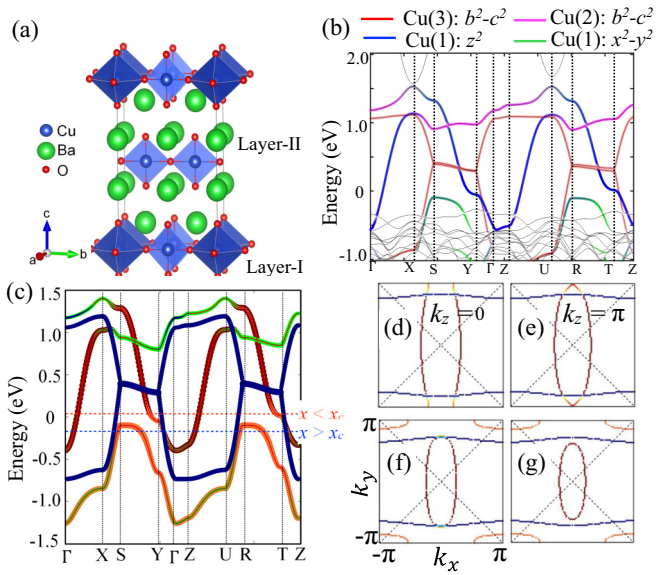

FIG. 1. (a) Crystal structure of $Ba_2CuO_{3.25}$. Layer I consists of copper in octahedral coordination [Cu(1)] and square planar complexes [Cu(2)], while layer II features Cu(3)/Cu(4) in square planar complexes, aligned along the b axis. (b) Atomic- and orbital-resolved bands are shown here [20]. (c) Orbital-resolved tight-binding bands of BCO. The red and blue dashed lines indicate two specific doping levels at E_F of 0.0778 and −0.0778 eV, based on rigid band approximations. These correspond to doping levels of $x = 0.24$ and 0.37, respectively. The critical doping level, where superconducting (SC) pairing symmetry transitions from singlet to triplet, is shown in Fig. 5. The critical values are $x_c = 0.29$ and 0.33 for $J_H = 0$ and $J_H \neq 0$, respectively. Fermi surfaces are shown at two different k_z cuts (0 and π) for two different doping levels, $x < x_c$ in (d) and (e) and $x > x_c$ in (f) and (g), respectively. The color scheme for different orbitals is d_{z^2} (brick red), $d_{x^2\text{-}y^2}$ (orange), Cu(2)-$d_{b^2\text{-}c^2}$(green), and Cu(3)/Cu(4)- $d_{b^2\text{-}c^2}$ (navy blue).

symmetry across the entire range of hole doping. We ascertain that, below a critical doping threshold (x_c), the SC pairing symmetry predominantly exhibits the conventional $d_{x^2\text{-}y^2}$ type. However, with increased doping, the SC pairing symmetry transitions to a multiband triplet solution. Notably, this feature demonstrates a significant robustness against Hund's coupling. This change in pairing symmetry we attribute to the interorbital nesting vectors that connect the d_{z^2} and $d_{x^2\text{-}y^2}$ FSs. While such triplet symmetry has not yet been observed in $Ba_2CuO_{3.2}$, our findings suggest that, through chemical doping or the application of pressure, this type of SC gap structure could be realized in future experiments.

The rest of this paper is organized as follows: In Sec. II, we provide a summary of the tight-binding (TB) model, along with the mechanisms underlying the multiband RPA spin-fluctuation approach. In Sec. III, we delve into the FS topology, examining the nesting profile, RPA spin susceptibility, and pairing symmetry. This section also explores the variation in pairing strength as a function of doping and investigates the density of states (DOS) in the SC state. Finally, in Sec. IV, we give a comprehensive discussion and conclusion of our findings.

II. METHOD AND MODEL

A. TB model

We consider a 14-orbital, TB Hamiltonian that effectively replicates the low-energy DFT band structure [20]. In our model, the four Cu atoms in the unit cell contribute five Cu-d orbitals, while the adjacent oxygen atoms provide nine p orbitals. The orbital-weight contribution to the DFT results shows that oxygen bands lie deep inside the Fermi level. Using the Löwdin downfolding procedure, we integrate out the oxygen bands and obtain an effective five-band model Hamiltonian. A more comprehensive analysis of this contribution is available in Appendix. The Hamiltonian is expressed as follows:

$$H(\mathbf{k}) = \sum_{\alpha\beta} \sum_{\substack{\mathbf{k} \\ \sigma\in(\uparrow,\downarrow)}} [\xi_{\alpha\beta}(\mathbf{k}) + \mu_\alpha \delta_{\alpha\beta}] c^\dagger_{\mathbf{k},\alpha,\sigma} c_{\mathbf{k},\beta,\sigma}, \quad (1)$$

where $\xi_{\alpha\beta}(\mathbf{k})$ is the TB matrix element fitted with the DFT bands. Fermion creation and annihilation operators are denoted by $c^\dagger_{\mathbf{k},\alpha,\sigma}$ and $c_{\mathbf{k},\beta,\sigma}$, respectively. The on-site energy for orbital α is μ_α

B. Multiband RPA susceptibility

We use the multiband Hubbard model to study the topology of the FS and corresponding spin-fluctuation potential. The Hamiltonian of the Hubbard model is given by [22]

$$H_{\text{int}} = \sum_{\alpha,\mathbf{q}} U n_{\alpha\uparrow}(\mathbf{q}) n_{\alpha\downarrow}(-\mathbf{q}) + \sum_{\alpha\neq\beta} \sum_{\mathbf{q}} \frac{V}{2} n_\alpha(\mathbf{q}) n_\beta(-\mathbf{q}) - \sum_{\alpha\neq\beta} \sum_{\mathbf{q}} \frac{J_H}{2} \mathbf{S}_\alpha(\mathbf{q}) \cdot \mathbf{S}_\beta(-\mathbf{q}), \quad (2)$$

where U and V are the intraorbital and interorbital Hubbard interactions between Cu-d orbitals, and J_H is the Hund's coupling.

Using perturbative expansion of the spin density and charge-density correlation function, we obtain RPA spin and charge susceptibilities:

$$\tilde{\chi}_{s/c}(\mathbf{q}) = \tilde{\chi}_0(\mathbf{q})[\tilde{\mathbb{I}} \mp \tilde{U}_{s/c} \tilde{\chi}_0(\mathbf{q})]^{-1}. \quad (3)$$

The nonzero components of on-site Hubbard interactions for spin and charge fluctuation are $\tilde{U}_s$ and $\tilde{U}_c$ [17,22]. The bare susceptibility is enhanced at the nesting wave vector which leads to a corresponding enhanced peak in the RPA spin susceptibility. The overall momentum space structure of the susceptibility can, in general, be more complex in multiorbital systems owing to the presence of matrix elements. In general, due to the presence of $(1 - \tilde{U}\chi_0)$ in the denominator for the RPA spin susceptibility, the contribution from the spin channel is enhanced compared with the charge channel that contains a $(1 + \tilde{U}\chi_0)$ contribution.

C. SC pairing symmetry

SC pairing in Cu-d electrons is mediated via spin fluctuations [20]. We calculate the spin-fluctuation pairing potential

by expanding the H_{int} from Eq. (2) into a perturbation series and collecting bubble and ladder diagrams. The effective Hamiltonian we obtain as [17,23]

$$H_{\text{eff}} = \sum_{\alpha\beta\gamma\delta}\sum_{\mathbf{kq},\sigma\sigma'} \Gamma^{\gamma\delta}_{\alpha\beta}(\mathbf{q}) c^{\dagger}_{\alpha\sigma}(\mathbf{k}) c^{\dagger}_{\beta\sigma'}(-\mathbf{k}) c_{\gamma\sigma'}(-\mathbf{k}-\mathbf{q}) \times c_{\delta\sigma}(\mathbf{k}+\mathbf{q}). \quad (4)$$

Here, the pairing potential is a tensor of four orbital indices. For singlet and triplet channels, the spin-fluctuation pairing potential is given by [22,24–46]

$$\tilde{\Gamma}_S(\mathbf{q}) = \tfrac{1}{2}[3\tilde{U}_s\tilde{\chi}_s(\mathbf{q})\tilde{U}_s - \tilde{U}_c\tilde{\chi}_c(\mathbf{q})\tilde{U}_c + \tilde{U}_s + \tilde{U}_c], \quad (5a)$$

$$\tilde{\Gamma}_T(\mathbf{q}) = -\tfrac{1}{2}[\tilde{U}_s\tilde{\chi}_s(\mathbf{q})\tilde{U}_s + \tilde{U}_c\tilde{\chi}_c(\mathbf{q})\tilde{U}_c]. \quad (5b)$$

Using a unitary transformation, we obtain pairing potential in the band basis:

$$\tilde{\Gamma}_{\mu\nu}(\mathbf{k},\mathbf{q}) = \sum_{\alpha\beta\gamma\delta} \Gamma^{\gamma\delta}_{\alpha\beta}(\mathbf{q}) \psi^{\mu\dagger}_{\alpha}(\mathbf{k}) \psi^{\mu\dagger}_{\beta}(-\mathbf{k}) \psi^{\nu}_{\gamma}(-\mathbf{k}-\mathbf{q}) \times \psi^{\nu}_{\delta}(\mathbf{k}+\mathbf{q}), \quad (6)$$

where (μ, ν) represent the band indices, and $\psi^{\mu}_{\alpha}(\mathbf{k})$ is the eigenvector component corresponding to orbital α, band μ and calculated at the wave vector $\mathbf{k}$. We obtain SC pairing symmetry by solving the linearized gap equation:

$$\Delta_{\mu}(\mathbf{k}) = -\lambda\frac{1}{N}\sum_{\nu,\mathbf{q}} \Gamma'_{\mu\nu}(\mathbf{k},\mathbf{q})\Delta_{\nu}(\mathbf{k}+\mathbf{q}), \quad (7)$$

where $\Gamma'_{\mu\nu}(\mathbf{k},\mathbf{q}) = \frac{\tilde{\Gamma}_{\mu\nu}(\mathbf{k},\mathbf{q})}{|v^{\nu}_{\mathbf{k}'}|}$, where $v^{\nu}_{\mathbf{k}'}$ is the Fermi velocity at $\mathbf{k}' = \mathbf{k}+\mathbf{q}$ for band ν. Here, λ is known as a SC coupling constant. By solving Eq. (7), we obtain the pairing eigenfunction for the largest eigenvalue. This largest eigenvalue determines the stability of SC gap function $\Delta(\mathbf{k})$ [32].

The unconventional SC within spin-fluctuation theory originates from a repulsive interaction that usually favors a sign change of the SC gap over the FS. Since χ_s [see Eq. (3)] is positive and larger than χ_c, the pairing potential in Eq. (5a) is repulsive. The only possible solution of the gap equation for repulsive interaction is when Δ [see Eq. (7)] changes sign between momentum vectors $\mathbf{k}$ and $\mathbf{k}+\mathbf{Q}$. This leads to an anisotropic solution of the gap function in the momentum space whose underlying symmetry transforms according to the irreducible representation of the crystal point group symmetry.

III. RESULTS

A. Electronic structure

In this paper, we begin by analyzing the electronic structure and FS topology at two distinct doping levels. We have effectively determined the doping level of our material by integrating the DOS up to the Fermi energy. For this purpose, we have adopted a weak coupling approach, so the band structure only undergoes slight modifications with respect to changes in electron occupancy. This assumption is based on the principle of the rigid band shift approximation, which posits that the overall band structure remains relatively unchanged even as the doping level varies. We choose two representative doping levels $x = 0.24$ and 0.37, corresponding to Fermi energies

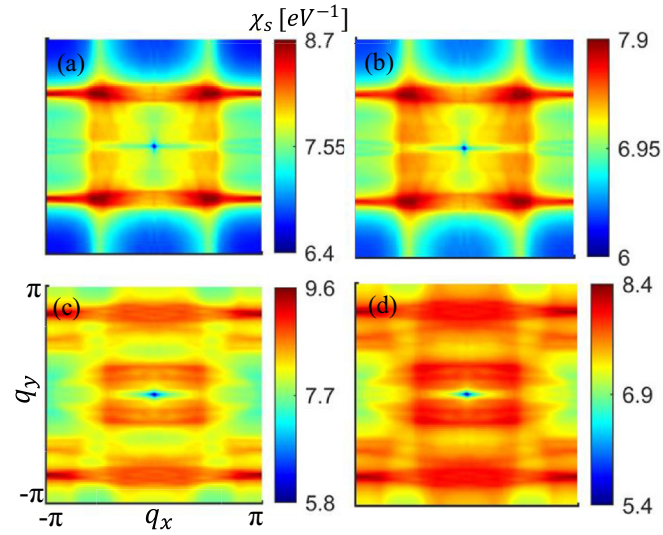

FIG. 2. (a)–(d) Physical random phase approximation (RPA) spin susceptibilities for two representation dopings. (a) and (b) are for $x < x_c$ with $J_H = 0$ and $\frac{U}{3}$, respectively. (c) and (d) are for $x > x_c$ with $J_H = 0$ and $\frac{U}{3}$, respectively.

(E_F) of 0.0778 and −0.0778 eV, respectively. The electronic band structures are depicted in Fig. 1(c). The red and blue horizontal dashed lines in Fig. 1(c) denote the low ($x = 0.24$) and high ($x = 0.37$) doping values, respectively. Our findings reveal that increasing hole doping leads to a reduction in the electron filling of the $d_{x^2\text{-}y^2}$ orbital. This creates additional hole pockets reminiscent of cuprate superconductors [17]. Notably, when the $d_{x^2\text{-}y^2}$ hole pocket becomes fully depleted, the FS is predominantly characterized by open electronlike pockets of d_{z^2} at $k_z = 0$ and closed electron pockets at $k_z = \pi$, with an enhanced contribution from $d_{b^2\text{-}c^2}$ orbitals on the open electron pockets persisting across the entire range of hole doping. Experimentally, the FS results can be corroborated by angle-resolved photoemission spectroscopy (ARPES) measurements conducted on BCO samples. Intriguingly, the presence of the hole pocket introduces additional nesting vectors, absent in the 40% hole-doping regime. In the following sections, we will demonstrate that these alterations in the $d_{x^2\text{-}y^2}$ FS significantly impact the overall pairing potential and, consequently, the pairing symmetry within the BCO system.

B. Evolution of FS nesting with doping

In the following section, we delve into the evolution of the FS nesting profile as a function of hole-doping concentration. For this purpose, we compute the RPA spin susceptibility, as shown in Fig. 2 for $q_z = 0$, and orbital-resolved components in Fig. 3. At low doping, FS has a mixed character of d_{z^2} and $d_{x^2\text{-}y^2}$ orbitals near the $(0, \pi)$ region. RPA susceptibility of the $d_{x^2\text{-}y^2}$ orbital is much lower than the interorbital contribution, as evident from Figs. 3(b) and 3(c). We have found a pronounced peak at the physical spin susceptibility near the $\pm(\pi-\delta, \pi-\delta)$ wave vector, in Fig. 2, which we posit to be a precursor to a $d_{x^2-y^2}$-type SC gap.

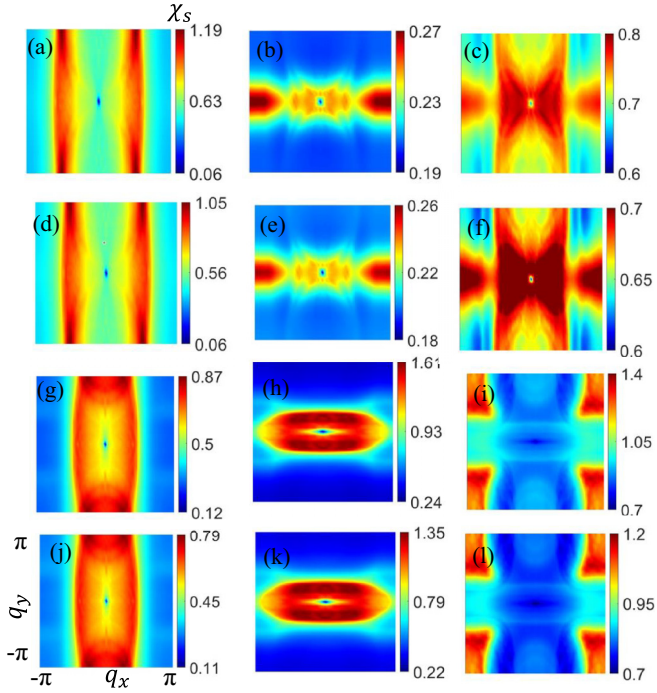

FIG. 3. (a)–(l) Orbital-resolved random phase approximation (RPA) spin susceptibilities for two representation dopings. Columns 1 and 2 belong to intraorbital (χ_{11}^{11}, χ_{22}^{22}) and column 3 is for interorbital (χ_{12}^{12}) contributions. Row 1 is for $x < x_c$ with $J_H = 0$, row 2 for $x < x_c$ with $J_H = \frac{U}{3}$, row 3 for $x > x_c$ with $J_H = 0$, and row 4 for $x > x_c$ with $J_H = \frac{U}{3}$.

The FS displays a k_z dependence, as depicted in Figs. 1(d)–1(g). However, the distribution of orbital weight across the Fermi level is such that the RPA spin susceptibility exhibits negligible q_z dependence. Consequently, we have focused solely on the $q_z = 0$ components in our susceptibility calculations. With increasing hole doping, in addition to the smaller electronlike pocket at the center of the Brillouin zone (BZ), an additional hole pocket with $d_{x^2\text{-}y^2}$ character emerges near the corners of the BZ (see Fig. 1). This new hole pocket, reminiscent of typical cuprate superconductors, ives a nesting vector of (π, π) to the CuO_4 plane. However, in BCO, because of the structural anisotropy (relative to Ba_2CuO_4), the hole pocket significantly alters the nesting vector, as demonstrated in the susceptibility plot in Figs. 2(c) and 2(d). Moreover, there is a notable reversal in the contributions of the $d_{x^2\text{-}y^2}$ and d_{z^2} orbitals to the intraorbital RPA susceptibility components in Figs. 3(g) and 3(h). The contribution of the intraorbital $d_{x^2\text{-}y^2}$ is marginally more significant than the interorbital susceptibility, which in turn correlates with a weaker d_{z^2} intraorbital susceptibility in Figs. 3(g)–3(i).

Figures 2(b) and 2(d) demonstrate the influence of Hund's coupling in diminishing the effectiveness of charge screening, together with their orbital-resolved components in Figs. 3(d)–3(f) and Figs. 3(j)–3(l). It is noteworthy that, in the absence of Hund's coupling, the peak value of the RPA spin susceptibility is larger, yet the overall nesting vector remains unchanged. Hence, we expect that the nodal structure of the SC gap does not change. Indeed, as will be demonstrated in Fig. 4, the symmetry of the SC gap does not vary for a given doping

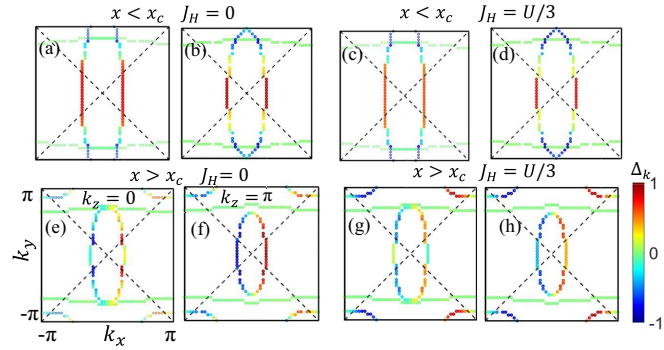

FIG. 4. (a)–(h) Computed pairing eigenfunction $\Delta(\mathbf{k})$ for the leading eigenvalue, plotted on the corresponding Fermi surfaces (FSs), for two representative values of doping (x). x_c is the critical value of the doping at which the leading superconducting (SC) gap changes from singlet to triplet pairing.

level. However, since the SC pairing potential is directly proportional to the strength of the RPA spin susceptibility, the strength of the pairing symmetry is attenuated in the presence of Hund's coupling.

C. SC properties

We now turn our attention to the doping dependence of SC in BCO. We include doping levels comparable with those considered in our susceptibility discussions. In Fig. 4, we present a plot of the SC gap on the FS, highlighting the largest pairing eigenvalue. The color bar in this figure illustrates the sign change in the SC gap function. Two distinct solutions emerge at varying doping values. Our results indicate that the singlet potential solution of Eq. (5a) exhibits the highest pairing eigenvalue (λ) at lower doping levels. Conversely, at higher doping levels, the triplet channel, Eq. (5b), gives the largest pairing strength.

As discussed earlier in the context of Fig. 2, at low doping levels, the FS nesting at $(\pi - \delta, \pi - \delta)$ significantly contributes to the RPA spin susceptibility. The FS exhibits D_{2h} symmetry, which is mirrored in the solution of the SC pairing potential. For doping levels >40%, the nesting condition within the CuO_6 octahedra fosters a pairing symmetry that fulfills the relation $\Delta(k + Q_1) = -\Delta(k)$ for the SC gap function, where $Q_1 = (\pi - \delta, \pi - \delta)$. At higher doping values ($x > x_c$), the uniaxial nesting condition arising from the $d_{x^2\text{-}y^2}$ orbital yields a nesting vector $Q_2 = (\pi - \delta, q_y \approx \text{small})$, affecting all Fermi momentum vectors. In this scenario, the FS leads to a gap function with a $\sin(k_x)$ structure. This corresponds to the triplet solution that emerges when the hole pocket crosses the VHS point from below. Consequently, in the overdoped region of BCO, we observe a triplet p-wave solution.

Next, we show the highest pairing eigenvalue across the entire hole-doped region, as depicted in Fig. 5. The selection of interaction parameters is chosen from the Stoner criterion, which is essential for fulfilling the normal state paramagnetic solution. SC pairing strength λ decreases with increased doping. This behavior remains robust against Hund's coupling. Hence, the doping dependence of λ is fundamentally linked

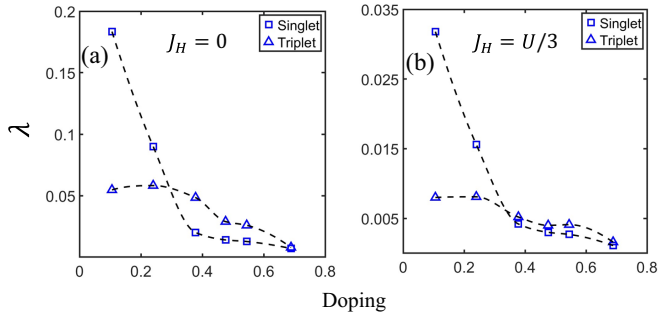

FIG. 5. (a) and (b) Doping-dependent superconducting (SC) coupling constant λ for BCO for a choice of $J_H = 0$ or $\frac{U}{3}$ eV.

to the FS nesting properties. The observed decrease in λ with hole doping is elucidated by examining the orbital-resolved DOS for BCO [20]. With hole doping, the DOS of the $d_{x^2\text{-}y^2}$ orbital increases, approaching the VHS, while the DOS of the d_{z^2} orbital diminishes. Additionally, a comparative analysis of the FS volumes in two doping regions indicates an increase in FS volume with enhanced electron filling. This contributes significantly to the calculations of λ using Eq. (7). The evolution of FS with doping is nonmonotonic, marked by the emergence of new orbitals ($d_{x^2\text{-}y^2}$). Within the framework of weak-coupling theory, the orbital-resolved SC gap is also expected to form in these new orbitals.

The SC pairing symmetry changes from a singlet to a triplet type as the system approaches the Lifshitz transition [see Figs. 4(a) and 4(e)]. The electronic structure, shown in Figs. 1(d) and 1(f), indicates that the Lifshitz transition occurs near a doping level of $x \approx 0.38$. At this critical doping, an additional hole Fermi pocket emerges, which is notably derived from the Cu(1) $d_{x^2\text{-}y^2}$ orbital. The emergence of a hole pocket significantly alters the FS nesting profile; hence, both the SC pairing strength and the gap symmetry change significantly due to the proximity of this Lifshitz transition.

D. SC spectral function

In the preceding section, we derived the SC gap $\Delta_\mu(\mathbf{k})$ from the spin-fluctuation mechanism by solving the linearized gap equation on the FS. However, to calculate the DOS in the SC state (SC-DOS), it is necessary to ascertain the gap across the entire BZ. Consequently, we employ the radial basis function (RBF) method [47] to extrapolate the gap data to encompass all BZ data points for varying k_z values. Following the extrapolation, we formulate the full mean-field Hamiltonian in the Nambu-Gorkov basis $\Psi_\mathbf{k} = (\phi_{\mathbf{k}\sigma}, \phi^\dagger_{-\mathbf{k}-\sigma})^T$, where $\phi_{\mathbf{k}\sigma}$ is composed of the Cu(1) $d_{z^2}/d_{x^2\text{-}y^2}$, Cu(2) $d_{b^2\text{-}c^2}$, and Cu(3)/Cu(4) $d_{b^2\text{-}c^2}$ states. Using this, we construct the mean-field Hamiltonian:

$$H_{\mathrm{SC}} = \begin{bmatrix} H(\mathbf{k}) & \tilde{\Delta}(\mathbf{k}) \\ \tilde{\Delta}^\dagger(-\mathbf{k}) & -H^\dagger(-\mathbf{k}) \end{bmatrix}. \tag{8}$$

We identify five distinct gap solutions, $\tilde{\Delta}(\mathbf{k})$ as indicated in Eq. (7), corresponding to five different orbitals coming from

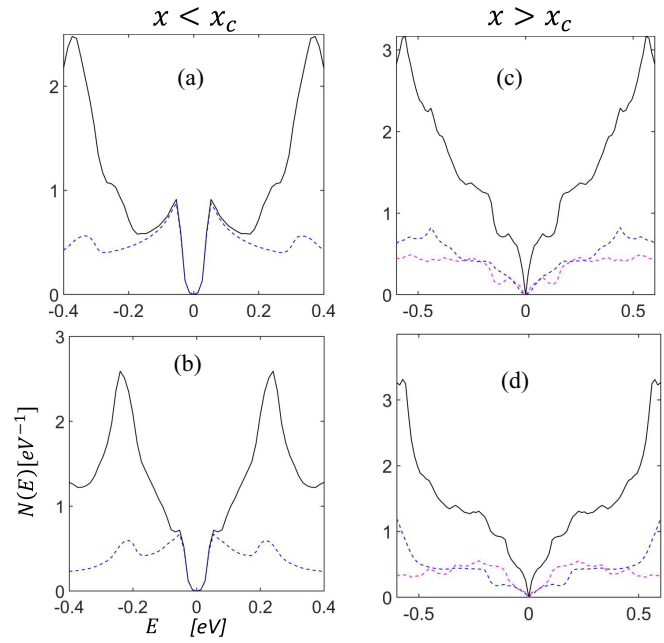

FIG. 6. (a)–(d) Total density of states (DOS) and orbital-resolved DOS for the superconducting (SC) state plotted for two representative values of doping (x). (a) and (b) are for $x < x_c$ with $J_H = 0$ and $\frac{U}{3}$, respectively. (c) and (d) are for $x > x_c$ with $J_H = 0$ and $\frac{U}{3}$, respectively. Blue and magenta dashed lines denotes contributions from the d_{z^2} and $d_{x^2\text{-}y^2}$ orbitals, respectively.

the octahedra and chainlike states of BCO:

$$\tilde{\Delta}(\mathbf{k}) = \begin{bmatrix} \Delta_1(\mathbf{k}) & . & . & . & . \\ . & \Delta_2(\mathbf{k}) & . & . & . \\ . & . & \Delta_3(\mathbf{k}) & . & . \\ . & . & . & \Delta_4(\mathbf{k}) & . \\ . & . & . & . & \Delta_5(\mathbf{k}) \end{bmatrix}. \tag{9}$$

As illustrated in Figs. 4(a)–4(d), Cu(1) d_{z^2} and Cu(3) $d_{b^2\text{-}c^2}$ orbitals manifest exclusively for $x < x_c$ (singlet case). For higher doping levels, $x > x_c$ (triplet case) in addition to the d_{z^2} orbital, and the $d_{x^2\text{-}y^2}$ orbital of Cu(1) significantly contributes to the spin-fluctuation gap equation.

In the SC state, the spectral function is determined by using the mean-field Hamiltonian, as specified in Eq. (8). We derive the spectral functions using

$$\tilde{A}(\mathbf{k}, E) = -\frac{1}{\pi}\mathrm{Im}\left[\frac{1}{(E + i\delta)I - H_{\mathrm{SC}}}\right]. \tag{10}$$

Here, δ is a small positive number introduced during the analytic continuation of the Matsubara frequencies, and E represents the energy of Bogoliubov quasiparticles. Further, we define the SC-DOS as $N(E) = \frac{1}{\Omega_{\mathrm{BZ}}}\sum_\mathbf{k} \tilde{A}(\mathbf{k}, E)$, where Ω_{BZ} is the total number of k points in the BZ. In Fig. 6, we illustrate the SC-DOS for both the singlet and triplet SC channels.

In the low-hole-doping regime ($x < x_c$), electron pockets at the Fermi level are predominantly derived from the Cu(1) d_{z^2} and Cu(3) $d_{b^2\text{-}c^2}$ orbitals within the singlet channel. In contrast, the $d_{x^2\text{-}y^2}$ orbitals of Cu(1) and the planar atoms of

Cu(2)/Cu(4) make minimal contributions to SC. On the other hand, in the high-hole-doping regime ($x > x_c$), the development of an additional hole pocket, associated with the $d_{x^2\text{-}y^2}$ orbital of Cu(1), supports the triplet SC channel. This results in a notable variation in the SC gap structure across these doping levels. Additionally, the impact of Hund's coupling on the SC-DOS has been demonstrated in Figs. 6(b) and 6(d), further elucidating the complex interplay of electronic states in SC.

In the presence of Hund's coupling, the V-shaped feature is prominent. Otherwise, the DOSs have a mixed V- and U-shaped characters. The robustness of this DOS feature against variations in Hund's coupling is significant. However, the DOS differences between singlet and triplet states are primarily attributed to the multiband structure of the SC-gap function. The observed V-shaped feature suggests a nodal gap structure. The residual DOS is attributable to the SC originating predominantly from two (or three) orbitals in the singlet (or triplet) channel; additionally, the hopping parameter is substantially larger than the maximum of the SC gap across the BZ. The SC gap diminishes exponentially faster toward the BZ boundary compared with the hopping parameter.

The orbital-resolved SC-DOS is sensitive to nodal structures but does not inherently distinguish between singlet and triplet SC states. However, in techniques such as scanning tunneling microscopy (STM), which are both local and surface sensitive, the importance of orbital-resolved SC-DOS is emphasized. Given that the contribution from the d_{z^2} orbital is significantly larger away from the surface, it becomes a critical factor for direct observations in STM experiments. At low energies, the SC-DOS of the d_{z^2} orbital (ρ_{z^2}), as illustrated in Figs. 6(a) and 6(b), exhibits an energy dependence that is more quadratic or of a higher power. This behavior suggests the presence of a point node or a significantly anisotropic gap contribution from this orbital. In contrast, ρ_{z^2} in the triplet state [see Figs. 6(c) and 6(d)] exhibits a more linear energy dependence, indicative of line node contributions. Such distinctions in the SC-DOS between the spin singlet and triplet SC gaps are anticipated to be detectable in STM experiments.

IV. DISCUSSIONS AND CONCLUSIONS

We have identified a triplet p-wave pairing in BCO, occurring at hole-doping levels significantly above the conventional optimal doping range for cuprate superconductors. This contrasts with other cuprates, where the Cu-$d_{x^2\text{-}y^2}$ orbital typically leads to d-wave pairing due to the (π, π) nesting vector. The key difference in BCO lies in the octahedral compression, which suppresses the $d_{x^2\text{-}y^2}$ orbital relative to the d_{z^2} orbital. The absence of $d_{x^2\text{-}y^2}$ changes the antiferromagnetic nesting vector differently than (π, π). The nesting vector is changed by shifts in the Fermi level, enabling the emergence of $d_{x^2\text{-}y^2}$ SC at lower doping levels. The absence of the $d_{x^2\text{-}y^2}$ orbital due to octahedral compression can be compensated by shifting above the VHS point through a rigid band shift. This adjustment introduces an additional hole pocket, which in turn suppresses the RPA susceptibility of the d_{z^2} orbital, previously dominant in the absence of $d_{x^2\text{-}y^2}$. Since the spin-fluctuation pairing potential is directly proportional to the RPA spin susceptibility, there is now a substantial contribution at the $Q_2 = (\pi - \delta, q_y \approx \text{small})$ nesting vector. Consequently, the SC gap function exhibits a change in sign corresponding to the reversal of the momentum vector.

Experimentally, the Andreev bound states manifests as zero bias peaks (ZBPs) in tunneling experiments [48–50]. This ZBP can be used as a distinguishing feature between singlet and triplet SC states, as demonstrated in our doping-dependent pairing calculations. For a (1,0,0) surface orientation, a ZBP is expected to form in the triplet state due to the antisymmetric nature of the gap function $[\Delta(k_x, k_y, k_z) = -\Delta(-k_x, k_y, k_z)]$, whereas such a peak is not anticipated in the singlet state, where the gap function is symmetric $[\Delta(k_x, k_y, k_z) = \Delta(-k_x, k_y, k_z)]$. Conversely, for a (0,1,0) surface, a ZBP will not form for either the spin-singlet or spin-triplet states. Therefore, the presence or absence of a ZBP at the corresponding surface in BCO materials offers a viable method for identifying the underlying SC state.

Triplet odd-parity SC exhibits a range of fascinating applications, including in superconductor/ferromagnet heterostructures and topological SC, leading to the Majorana modes [51], etc. Notably, triplet odd-parity SC has been recently observed in the heavy fermion superconductor $CeRh_2As_2$ [52]. Additionally, a handful of studies on cuprates have indicated the presence of p-wave SC [53–55]. However, similar results in cuprates is still lacking. In this context, our results could serve as motivation for experimental investigations into the signatures of triplet SC in doped BCO. Such investigations might include field angle and magnetic field measurements, nuclear magnetic resonance (NMR), Knight shift measurements, and ARPES.

ACKNOWLEDGMENTS

This work is funded by Science and Engineering Research Board of Department of Science and Technology (SERB-DST), India through Grant No. CRG/2020/004330. S.M. acknowledges the financial support by SERB-DST, India through the MATRICS Grant No. MTR/2020/000524.

APPENDIX: DETAILS OF THE TB HAMILTONIAN

The matrix representation of the Slater-Koster tight-binding (SK-TB) model Hamiltonian of BCO3.25 is shown in Eq. (2). Here, the submatrix H of layer I in basis set order d_{z^2}, $d_{x^2\text{-}y^2}$, $d_{x^2\text{-}y^2}$, p_x, p_z, p_z, p_y, and p_y is [20]

$$H_{l1} = \begin{pmatrix} \xi_1 & \xi_{1,2} & \xi_{1,3} & \xi_{1,4} & \xi_{1,5} & 0 & \xi_{1,7} & 0 \\ & \xi_2 & \xi_{2,3} & \xi_{2,4} & \xi_{2,5} & \xi^*_{2,5} & 0 & 0 \\ & & \xi_3 & 0 & \xi^*_{2,5} & \xi_{2,5} & 0 & 0 \\ & & & \mu^{(3)} & 0 & 0 & 0 & 0 \\ & & \text{H.c.} & & \mu^{(1)} & 0 & 0 & 0 \\ & & & & & \mu^{(1)} & 0 & 0 \\ & & & & & & \mu^{(1)} & 0 \\ & & & & & & & \mu^{(1)} \end{pmatrix} \quad \text{(A1)}$$

where H.c. denotes the Hermitian conjugate of the upper-triangular matrix.

The Hamiltonian submatrix for layer II in orbital basis set of $d_{x^2\text{-}y^2}$, $d_{x^2\text{-}y^2}$, p_z, p_z, p_y, and p_y is given as

$$H_{l2} = \begin{pmatrix} \xi_4 & \xi_{4,5} & \xi_{4,6} & 0 & 0 & 0 \\ & \xi_5 & 0 & \xi_{4,6} & 0 & 0 \\ & & \mu^{(7)} & 0 & 0 & 0 \\ & \text{H.c.} & & \mu^{(7)} & 0 & 0 \\ & & & & \mu^{(7)} & 0 \\ & & & & & \mu^{(7)} \end{pmatrix} \tag{A2}$$

Further, the Hamiltonian submatrix containing the interaction between layers I and II is

$$H_{l1-l2} = \begin{bmatrix} 0 & 0 & 0 & 0 & \xi_2^{12} & -(\xi_2^{12})^* \\ 0 & 0 & 0 & 0 & 0 & 0 \\ \xi_1^{12} & (\xi_1^{12})^* & 0 & 0 & \xi_3^{12} & -(\xi_3^{12})^* \\ 0 & 0 & 0 & 0 & 0 & 0 \\ : & & & : & & : \\ 0 & 0 & 0 & 0 & 0 & 0 \end{bmatrix}. \tag{A3}$$

The components of the Hamiltonian matrices are found to be,

$$\xi_1 = t^{(5)}\cos(k_x) + \mu^{(4)} + t^{(15)}\cos(k_y) - 0.1\cos(2k_x), \tag{A4}$$

$$\xi_2 = t^{(10)}\cos(ky) + t^{(11)}\cos(k_x) + \mu^{(2)}, \tag{A5}$$

$$\xi_3 = \xi_2 + \mu^{(5)}, \tag{A6}$$

$$\xi_4 = t^{(14)}\cos(k_x) + \mu^{(6)}, \tag{A7}$$

$$\xi_5 = \xi_4 + 0.02, \tag{A8}$$

$$\xi_{1,2} = t^{(3)}\cos(k_x) + t^{(9)}\cos(k_y), \tag{A9}$$

$$\xi_{1,3} = t^{(4)}\exp\left(\frac{ik_y}{4}\right), \tag{A10}$$

$$\xi_{2,3} = t^{(1)}\cos\left(\frac{k_y}{2}\right), \tag{A11}$$

$$\xi_{1,4} = it^{(8)}\sin\left(\frac{k_x}{2}\right), \tag{A12}$$

$$\xi_{1,5} = it^{(8)}\sin\left(\frac{k_y}{4}\right), \tag{A13}$$

$$\xi_{1,7} = it^{(6)}\sin(0.156k_z), \tag{A14}$$

$$\xi_{2,4} = it^{(7)}\sin\left(\frac{k_x}{2}\right), \tag{A15}$$

$$\xi_{2,5} = t^{(4)}\exp\left(\frac{ik_y}{4}\right), \tag{A16}$$

$$\xi_{4,5} = t^{(12)}\cos\left(\frac{k_y}{2}\right), \tag{A17}$$

$$\xi_{4,6} = it^{(13)}\sin\left(\frac{k_y}{4}\right), \tag{A18}$$

$$\xi_1^{12} = 2t_{12}^{(1)}\exp\left(-\frac{ik_y}{4}\right)\cos\left(\frac{k_z}{2}\right)\cos\left(\frac{k_x}{2}\right), \tag{A19}$$

$$\xi_2^{12} = it_{12}^{(2)}\exp\left(\frac{ik_y}{4}\right)\sin\left(\frac{k_z}{3}\right)\cos\left(\frac{kx}{2}\right), \tag{A20}$$

$$\xi_3^{12} = it_{12}^{(2)}\exp\left(-\frac{ik_y}{4}\right)\sin\left(\frac{k_z}{3}\right)\cos\left(\frac{k_x}{2}\right). \tag{A21}$$

The TB parameters are $t^{(1-14)} = [0.9775,\ 0.0237,\ 0.3396,\ 0.005,\ -0.78,\ 0.2076,\ -0.46,\ 0.0,\ 0.035,\ -0.119,\ -0.074,\ 0.91,\ 0.6928,\ -0.054,\ -0.06]$, $\mu^{(1-7)} = [-0.74,\ -0.31,\ -1.24,\ 0.5,\ 1.18,\ 0.28,\ -1.64]$, and $t_{12}^{(1-2)} = [-0.02,\ -0.3]$. The Löwdin method used for the downfolding mechanism can be explained by

$$H_{\alpha,\beta}^{\text{downfold}} = H_{\alpha,\beta} + \sum_{I\neq\alpha}{}' \frac{H_{\alpha,I}(H_{\beta,I})^*}{H_{\alpha,\alpha} - H_{I,I}}. \tag{A22}$$

Here, $H_{\alpha,\beta}^{\text{downfold}}$ is the final 5×5 downfolded Hamiltonian, I denotes nine oxygen p orbitals, and α, β represents five Cu-d orbitals.

[1] C. C. Tsuei and J. R. Kirtley, Pairing symmetry in cuprate superconductors, Rev. Mod. Phys. **72**, 969 (2000).

[2] D. J. Scalapino, The case for $d_{x^2\text{-}y^2}$ pairing in the cuprate superconductors, Phys. Rep. **250**, 329 (1995).

[3] J. R. Kirtley, C. C. Tsuei, J. Z. Sun, C. C. Chi, L. S. Yu-Jahnes, A. Gupta, M. Rupp, and M. B. Ketchen, Symmetry of the order parameter in the high-T_c superconductor $YBa_2Cu_3O_{7-\delta}$, Nature (London) **373**, 225 (1995).

[4] D. H. Wu, J. Mao, S. N. Mao, J. L. Peng, X. X. Xi, T. Venkatesan, R. L. Greene, and S. M. Anlage, Temperature dependence of penetration depth and surface resistance of $Nd_{1.85}Ce_{0.15}CuO_4$, Phys. Rev. Lett. **70**, 85 (1993).

[5] S. M. Anlage, D. H. Wu, J. Mao, S. N. Mao, X. X. Xi, T. Venkatesan, J. L. Peng, and R. L. Greene, Electrodynamics of $Nd_{1.85}Ce_{0.15}CuO_4$: Comparison with Nb and $YBa_2Cu_3O_{7-\delta}$, Phys. Rev. B **50**, 523 (1994).

[6] A. Andreone, A. Cassinese, A. DiChiara, R. Vaglio, A. Gupta, and E. Sarnelli, Temperature dependence of the penetration depth in $Nd_{1.85}Ce_{0.15}CuO_{4-\delta}$, superconducting thin films, Phys. Rev. B **49**, 6392 (1994).

[7] C. W. Schneider, Z. H. Barber, J. E. Evetts, S. N. Mao, X. X. Xi, and T. Venkatesan, Penetration depth measurements for $Nd_{1.85}Ce_{0.15}CuO_4$ and NbCN thin films using a kinetic inductance technique, Physica C **233**, 77 (1994).

[8] A. Ino, C. Kim, M. Nakamura, T. Yoshida, T. Mizokawa, Z.-X. Shen, A. Fujimori, T. Kakeshita, H. Eisaki, and S. Uchida, Electronic structure of $La_{2-x}Sr_xCuO_4$ in the vicinity of the superconductor-insulator transition, Phys. Rev. B **62**, 4137 (2000).

[9] E. Razzoli, G. Drachuck, A. Keren, M. Radovic, N. C. Plumb, J. Chang, Y.-B. Huang, H. Ding, J. Mesot, and M. Shi, Evolution from a nodeless gap to $d_{x^2-y^2}$-wave in underdoped $La_{2-x}Sr_xCuO_4$, Phys. Rev. Lett. **110**, 047004 (2013).

[10] K. Tanaka, W. S. Lee, D. H. Lu, A. Fujimori, T. Fujii, Risdiana, I. Terasaki, D. J. Scalapino, T. P. Devereaux, Z. Hussain *et al.*, Distinct Fermi-momentum-dependent energy gaps in deeply underdoped Bi2212, Science **314**, 1910 (2006).

[11] I. M. Vishik, M. Hashimoto, R.-H. He, W.-S. Lee, F. Schmitt, D. Lu, R. G. Moore, C. Zhang, W. Meevasana, T. Sasagawa *et al.*, Phase competition in trisected superconducting dom, Proc. Natl. Acad. Sci. USA **109**, 18332 (2012).

[12] Y. Peng, J. Meng, D. Mou, J. He, L. Zhao, Y. Wu, G. Liu, X. Dong, S. He, J. Zhang *et al.*, Disappearance of nodal gap across the insulator-superconductor transition in a copper-oxide superconductor, Nat. Commun. **4**, 2459 (2013).

[13] K. M. Shen, T. Yoshida, D. H. Lu, F. Ronning, N. P. Armitage, W. S. Lee, X. J. Zhou, A. Damascelli, D. L. Feng, N. J. C. Ingle *et al.*, Fully gapped single-particle excitations in lightly doped cuprates, Phys. Rev. B **69**, 054503 (2004).

[14] D. Gustafsson, D. Golubev, M. Fogelström, T. Claeson, S. Kubatkin, T. Bauch, and F. Lombardi, Fully gapped superconductivity in a nanometre-size $YBa_2Cu_3O_{7-\delta}$ island enhanced by a magnetic field, Nat. Nanotechnol. **8**, 25 (2013).

[15] D. J. Scalapino, A common thread: The pairing interaction for unconventional superconductors, Rev. Mod. Phys. **84**, 1383 (2012).

[16] A. T. Rømer, A. Kreisel, I. Eremin, M. A. Malakhov, T. A. Maier, P. J. Hirschfeld, and B. M. Andersen, Pairing symmetry of the one-band Hubbard model in the paramagnetic weak-coupling limit: A numerical RPA study, Phys. Rev. B **92**, 224515 (2015).

[17] P. Adhikary and T. Das, Prediction of f-wave pairing symmetry in $YBa_2Cu_3O_{6+x}$ cuprates, Phys. Rev. B **101**, 214517 (2020).

[18] W. M. Li, J. F. Zhao, L. P. Cao, Z. Hu, Q. Z. Huang, X. C. Wang, Y. Liu, G. Q. Zhao, J. Zhang, Q. Q. Liu *et al.*, Superconductivity in a unique type of copper oxide, Proc. Natl. Acad. Sci. USA **116**, 12156 (2019).

[19] R. Fumagalli, A. Nag, S. Agrestini, M. Garcia-Fernandez, A. C. Walters, D. Betto, N. B. Brookes, L. Braicovich, K.-J. Zhou, G. Ghiringhelli *et al.*, Crystalline and magnetic structure of $Ba_2CuO_{3+\delta}$ investigated by x-ray absorption spectroscopy and resonant inelastic x-ray scattering, Physica C **581**, 1353810 (2021).

[20] P. Adhikary, M. Gupta, A. Chauhan, S. Satpathy, S. Mukherjee, and B. R. K. Nanda, Unique d_{xy} superconducting state in the cuprate $Ba_2CuO_{3.25}$, Phys. Rev. B **109**, L020505 (2024).

[21] P. Worm, M. Kitatani, J. M. Tomczak, L. Si, and K. Held, Hidden one-dimensional, strongly nested, and almost half-filled Fermi surface in Ba_2CuO_{3+y} superconductors, Phys. Rev. B **105**, 085110 (2022).

[22] S. Graser, T. A. Maier, P. J. Hirschfeld, and D. J. Scalapino, Near-degeneracy of several pairing channels in multiorbital models for the Fe-pnictides, New J. Phys. **11**, 025016 (2009).

[23] P. Adhikary, S. Bandyopadhyay, T. Das, I. Dasgupta, and T. Saha-Dasgupta, Orbital-selective superconductivity in a two-band model of infinite-layer nickelates, Phys. Rev. B **102**, 100501(R) (2020).

[24] D. J. Scalapino, E. Loh, Jr., and J. E. Hirsch, d-wave pairing near a spin-density-wave instability, Phys. Rev. B **34**, 8190(R) (1986).

[25] T. M. Rice and K. Ueda, Gutzwiller method for heavy electrons, Phys. Rev. B **34**, 6420 (1986).

[26] J. R. Schrieffer, *Theory of Superconductivity* (W. A. Benjamin, New York, 1964).

[27] J. R. Schrieffer, X. G. Wen, and S. C. Zhang, Dynamic spin fluctuations and the bag mechanism of high-T_c superconductivity, Phys. Rev. B **39**, 11663 (1989).

[28] P. Monthoux, A. V. Balatsky, and D. Pines, Toward a theory of high-temperature superconductivity in the antiferromagnetically correlated cuprate oxides, Phys. Rev. Lett. **67**, 3448 (1991).

[29] M. Sigrist and K. Ueda, Phenomenological theory of unconventional superconductivity, Rev. Mod. Phys. **63**, 239 (1991).

[30] J. C. Seamus Davis and D.-H. Lee, Concepts relating magnetic interactions, intertwined electronic orders, and strongly correlated superconductivity, Proc. Natl. Acad. Sci. USA **110**, 17623 (2013).

[31] T. Das, R. S. Markiewicz, and A. Bansil, Intermediate coupling model of the cuprates, Adv. Phys. **63**, 151 (2014).

[32] A. V. Chubukov, D. Pines, and J. Schmalian, A spin fluctuation model for d-wave superconductivity, in *The Physics of Superconductors*, edited by K. H. Bennemann and J. B. Ketterson (Springer, Berlin, 2003).

[33] I. I. Mazin, D. J. Singh, M. D. Johannes, and M. H. Du, Unconventional superconductivity with a sign reversal in the order parameter of $LaFeAsO_{1-x}F_x$, Phys. Rev. Lett. **101**, 057003 (2008).

[34] Zi.-J. Yao, J.-X. Li, and Z. D. Wang, Spin fluctuations, interband coupling and unconventional pairing in iron-based superconductors, New J. Phys. **11**, 025009 (2009).

[35] T. Das and A. V. Balatsky, Spin superconductor in ferromagnetic graphene, Phys. Rev. B **84**, 014521 (2011).

[36] A. Chubukov, Pairing mechanism in Fe-based superconductors, Annu. Rev. Condens. Matter Phys. **3**, 57 (2012).

[37] T. Takimoto, T. Hotta, and K. Ueda, Strong-coupling theory of superconductivity in a degenerate Hubbard model, Phys. Rev. B **69**, 104504 (2004).

[38] K. Kubo, Pairing symmetry in a two-orbital Hubbard model on a square lattice, Phys. Rev. B **75**, 224509 (2007).

[39] T. Das, J.-X. Zhu, and M. J. Graf, Theory of nodal $s^{\pm}$-wave pairing symmetry in the Pu-based 115 superconductor family, Sci. Rep. **5**, 8632 (2015).

[40] H. Ikeda, M.-To. Suzuki, and R. Arita, Emergent loop-nodal $s_{\pm}$-wave superconductivity in $CeCu_2Si_2$: Similarities to the iron-based superconductors, Phys. Rev. Lett. **114**, 147003 (2015).

[41] T. Nomoto and H. Ikeda, Exotic multigap structure in UPt_3 unveiled by a first-principles analysis, Phys. Rev. Lett. **117**, 217002 (2016).

[42] T. Nomoto and H. Ikeda, Symmetry-protected line nodes in non-symmorphic magnetic space groups: Applications to UCoGe and UPd_2Al_3, J. Phys. Soc. Jpn. **86**, 023703 (2017).

[43] J. Schmalian, Pairing due to spin fluctuations in layered organic superconductors, Phys. Rev. Lett. **81**, 4232 (1998).

[44] G. Saito and Y. Yoshida, Frontiers of organic conductors and superconductors, Chem. Rec. **11**, 124 (2011).

[45] T. Das and K. Dolui, Superconducting dome in MoS_2 and $TiSe_2$ generated by quasiparticle-phonon coupling, Phys. Rev. B **91**, 094510 (2015).

[46] A. Bhattacharyya, D. T. Adroja, K. Panda, S. Saha, T. Das, A. J. S. Machado, O. V. Cigarroa, T. W. Grant, Z. Fisk, A. D. Hillier *et al.*, Evidence of a nodal line in the superconducting gap symmetry of noncentrosymmetric $ThCoC_2$, Phys. Rev. Lett. **122**, 147001 (2019).

[47] https://people.sc.fsu.edu/~jburkardt/m_src/rbf_interp_2d/rbf_interp_2d.html.

[48] S. Kashiwaya and Y. Tanaka, Tunnelling effects on surface bound states in unconventional superconductors, Rep. Prog. Phys. **63**, 1641 (2000).

[49] S. V. Bakurskiy, A. A. Golubov, M. Yu. Kupriyanov, K. Yada, and Y. Tanaka, Anomalous surface states at interfaces in *p*-wave superconductors, Phys. Rev. B **90**, 064513 (2014).

[50] J. Y. T. Wei, N. C. Yeh, D. F. Garrigus, and M. Strasik, Directional tunneling and Andreev reflection on $YBa_2Cu_3O_{7-\delta}$ single crystals: Predominance of *d*-wave pairing symmetry verified with the generalized Blonder, Tinkham, and Klapwijk theory, Phys. Rev. Lett. **81**, 2542 (1998).

[51] Y.-F. Lv, W.-L. Wang, Y.-M. Zhang, H. Ding, W. Li, L. Wang, K. He, C.-L. Song, X.-C. Ma, and Q.-K. Xue, Experimental signature of topological superconductivity and Majorana zero modes on β-Bi_2Pd thin films, Sci. Bull. **62**, 852 (2017).

[52] J. F. Landaeta and K. Dolui, Field-angle dependence reveals odd-parity superconductivity in $CeRh_2As_2$, Phys. Rev. X **12**, 031001 (2022).

[53] Y.-M. Lu, T. Xiang, and D.-H. Lee, Can deeply underdoped superconducting cuprates be topological superconductors? Nat. Phys. **10**, 634 (2014).

[54] T. Das, Nodeless superconducting gap induced by odd parity pair density wave in underdoped cuprates, Ann. Phys. **420**, 168251 (2020).

[55] A. Gupta and D. Sa, Topological phase in a $d_{x^2-y^2} + (p + ip)$ superconductor in presence of spin-density-wave, Eur. Phys. J. B **89**, 24 (2016).